resulting images for scans parallel to the ridge tops (Fig. 4C) reveal uniformly enhanced signals near the triangular peaks. More importantly, cross-sectional scans (Fig. 4D) show that the response is high at this peak while remaining low along the smooth sides of the ridges and the valleys in between. Using the protocol and apparatus in (*28*), we quantified the SERS enhancement by comparing the Raman signal from neat benzenethiol with that from our monolayer-coated substrate (Fig. 4E). After correcting for the number of molecules, we determined an enhancement factor of 1.4×10^7. Because this represents an average over the entire surface, the actual enhancement near the ridge peak should be much higher.

Whereas bumps, ridges, and grooves are clearly useful for these types of applications, different structural elements are necessary for others. For example, a nanoscale hole surrounded by surface structures can allow enhanced transmission of electromagnetic waves through a metal film (*3*). Figure 2F shows that we can also create such holes in thin smooth silver films. A hexagonal array of deep circular pits was formed on a silicon wafer with nanosphere lithography. By evaporating silver on top of such pits and adding epoxy, a thin silver film with a hole array was obtained. Although only one side of this film is ultrasmooth, which would affect its transmission properties, an additional absorbing layer such as Cr could be added to the rough side to minimize its effects. A second useful element is the multilayer structure. For example, thin patterned films with alternating layers of metal and insulator can exhibit a negative refractive index (*29*), which can lead to new optical phenomena (*30*). Our approach can also yield such structures, called metamaterials. After evaporating a thin film of silver on patterned silicon templates, we deposited alternating layers of alumina and silver. Because silver adheres to alumina better than silicon, the entire stack could be removed with epoxy. For example, a bull's eye (Fig. 2G) and a bump array (fig. S7) could be easily obtained, both of which have potential use as superlenses (*30*). As long as the adhesion requirement is satisfied, other materials besides alumina are also possible. The resulting films can lead to a variety of useful optoelectronic devices, especially considering that they are formed on flexible substrates with built-in metal contacts.

These results indicate that template stripping can be combined with silicon microfabrication methods to create ultrasmooth patterned metals for plasmonics and metamaterials. Although extremely simple, it provides a route to fabricate integrated metallic multilayer structures with designed grooves, bumps, tips, and holes with controlled spacings and orientations, while simultaneously avoiding previous problems because of roughness and impurities.

References and Notes

1. H. Raether, *Surface Plasmons* (Springer, Berlin, 1988).
2. H. A. Atwater, *Sci. Am.* **296**, 56 (2007).
3. C. Genet, T. W. Ebbesen, *Nature* **445**, 39 (2007).
4. E. Ozbay, *Science* **311**, 189 (2006).
5. N. Engheta, *Science* **317**, 1698 (2007).
6. A. Polman, *Science* **322**, 868 (2008).
7. L. Yin *et al.*, *Nano Lett.* **5**, 1399 (2005).
8. E. J. R. Vesseur *et al.*, *Appl. Phys. Lett.* **92**, 083110 (2008).
9. M. Kuttge *et al.*, *Appl. Phys. Lett.* **93**, 113110 (2008).
10. D. Sarid, *Phys. Rev. Lett.* **47**, 1927 (1981).
11. B. D. Gates *et al.*, *Chem. Rev.* **105**, 1171 (2005).
12. Y. L. Loo, R. L. Willett, K. W. Baldwin, J. A. Rogers, *J. Am. Chem. Soc.* **124**, 7654 (2002).
13. G. Kumar, H. X. Tang, J. Schroers, *Nature* **457**, 868 (2009).
14. M. Hegner, P. Wagner, G. Semenza, *Surf. Sci.* **291**, 39 (1993).
15. M. Graca, J. Turner, M. Marshall, S. Granick, *J. Appl. Phys.* **102**, 064909 (2007).
16. B. Jung, W. Frey, *Nanotechnology* **19**, 145303 (2008).
17. W. Frey, C. K. Woods, A. Chilkoti, *Adv. Mater.* **12**, 1515 (2000).
18. See supporting material on *Science* Online.
19. P. Samori, J. Diebel, H. Lowe, J. P. Rabe, *Langmuir* **15**, 2592 (1999).
20. Q. B. Xu, I. Tonks, M. J. Fuerstman, J. C. Love, G. M. Whitesides, *Nano Lett.* **4**, 2509 (2004).
21. J. Henzie, E. S. Kwak, T. W. Odom, *Nano Lett.* **5**, 1199 (2005).
22. V. V. Temnov, U. Woggon, J. Dintinger, E. Devaux, T. W. Ebbesen, *Opt. Lett.* **32**, 1235 (2007).
23. J. T. van Wijngaarden *et al.*, *Appl. Phys. Lett.* **88**, 221111 (2006).
24. D. L. Mills, *Phys. Rev. B* **12**, 4036 (1975).
25. H. Shiba, M. Haraguchi, M. Fukui, *J. Phys. Soc. Jpn.* **63**, 1400 (1994).
26. A. J. Haes *et al.*, *MRS Bull.* **30**, 368 (2005).
27. C. L. Haynes, R. P. Van Duyne, *J. Phys. Chem. B* **107**, 7426 (2003).
28. K. C. Bantz, C. L. Haynes, *Langmuir* **24**, 5862 (2008).
29. G. Dolling, M. Wegener, S. Linden, *Opt. Lett.* **32**, 551 (2007).
30. D. R. Smith, J. B. Pendry, M. C. K. Wiltshire, *Science* **305**, 788 (2004).

31. We thank K. Bantz and C. Haynes for help with SERS measurements and B. Carlson for help with x-ray photoelectron spectroscopy. This work was supported by the U.S. Department of Energy (grant DE-FG02-06ER46438) and used resources in the Institute of Technology at the University of Minnesota, including the Nanofabrication Center, which receives partial support from NSF through the National Nanotechnology Infrastructure Network program, and the Characterization Facility, which has received capital equipment funding from NSF through the Materials Research Science and Engineering Center, Major Research Instrumentation, and Engineering Research Center programs. S.-H.O. acknowledges support from a Minnesota Partnership for Biotechnology Award and a 3M Non-Tenured Faculty Award. P.N. and N.C.L. acknowledge support from a University of Minnesota doctoral dissertation fellowship and an NIH Biotechnology training grant, respectively. The authors have applied for a patent on the fabrication methods described.

Supporting Online Material

www.sciencemag.org/cgi/content/full/325/5940/594/DC1
Materials and Methods
Figs. S1 to S7
Tables S1 to S3
References

7 April 2009; accepted 16 June 2009
10.1126/science.1174655

Probing Spin-Charge Separation in a Tomonaga-Luttinger Liquid

Y. Jompol,[1]* C. J. B. Ford,[1] J. P. Griffiths,[1] I. Farrer,[1] G. A. C. Jones,[1] D. Anderson,[1] D. A. Ritchie,[1] T. W. Silk,[2] A. J. Schofield[2]

In a one-dimensional (1D) system of interacting electrons, excitations of spin and charge travel at different speeds, according to the theory of a Tomonaga-Luttinger liquid (TLL) at low energies. However, the clear observation of this spin-charge separation is an ongoing challenge experimentally. We have fabricated an electrostatically gated 1D system in which we observe spin-charge separation and also the predicted power-law suppression of tunneling into the 1D system. The spin-charge separation persists even beyond the low-energy regime where the TLL approximation should hold. TLL effects should therefore also be important in similar, but shorter, electrostatically gated wires, where interaction effects are being studied extensively worldwide.

The effects of interactions are almost impossible to calculate in a general many-particle system, although they cannot be ignored. However, for a one-dimensional (1D) system, Luttinger, building on an approximation scheme of Tomonaga, constructed a soluble 1D model with infinite linear dispersion and a restricted set of interactions. The solution has the remarkable property that the excitations of spin and charge behave independently and move with different speeds. It has been argued (*1*) that all 1D metals are adiabatically continuous with the Tomonaga-Luttinger model at low energies, and hence spin-charge separation should be observable in real systems. Determining the extent of its applicability would provide a major test of more general methods of modeling interaction effects, with relevance to quantum devices and the theory of high-temperature superconductivity. Recent work (*2*) presents a more general theory of 1D systems with a nonlinear dispersion, but the effects of spin are not yet included.

Some properties of the Tomonaga-Luttinger liquid (TLL), such as power-law behavior, have been observed and studied in a variety of systems,

[1]Cavendish Laboratory, University of Cambridge, J. J. Thomson Avenue, Cambridge CB3 0HE, UK. [2]School of Physics and Astronomy, University of Birmingham, Edgbaston, Birmingham B15 2TT, UK.

*To whom correspondence should be addressed. E-mail: yodchay.jompol@cantab.net

such as carbon nanotubes (*3*) and edge states in the fractional quantum Hall regime (*4*), but these experiments have not directly resolved the dispersion of the excitations in a TLL. Only a few experiments have attempted to detect the spin-charge separation directly, for example, by photoemission spectroscopy (*5*–*7*) and tunneling spectroscopy between a pair of closely spaced cleaved-edge-overgrown quantum wires (*8*–*10*). The latter 1D-1D tunneling results are striking and provide some evidence of dispersing spinons and holons—the excitations of a TLL. However, in these experiments TLLs act as both probe and subject, so an independent study—in a different geometry—of the excitation spectrum is vital to be sure of the interpretation.

We use a 2D electron gas (2DEG) as the (well-understood) probe layer. Use of an array of highly regular wires averages out impurity, length-resonance, and charging effects, and measurements of power-law behavior and spin-charge separation can be made with just the lowest 1D subband, without electrons becoming localized. Interpretation of TLL results is thus much easier, and results obtained in the nonlinear regime, where the theory is much less well developed, can be directly interpreted as a modification of the 1D elementary excitations. Our 1D wires are formed using split gates, where the confinement is much weaker than in the overgrown wires, making the results relevant to a broad range of other devices. The tunneling current I between the 1D wires and an adjacent low-disorder layer containing a 2DEG depends on the overlap between the spectral functions of the two systems. This overlap is varied by using an in-plane magnetic field B perpendicular to the wires to offset the two spectral functions in k space by $\Delta k = eBd/\hbar$ along the wires, where d is the center-to-center tunneling distance between the two systems (*11*). By applying a positive bias V_{dc} to the 2DEG relative to the wires, electrons tunnel into excited states of the 2DEG, from matching states below the Fermi energy in the 1D wires, allowing investigation of the energy dependence. Thus, the 2D system acts as a spectrometer, and the differential conductance G displays resonant-tunneling peaks corresponding to overlapping points in the offset dispersion relations, where energy and momentum are conserved.

Our devices contain an array of about 350 extremely regular quantum wires in the upper layer of a GaAs-AlGaAs double-quantum-well (DQW) structure (Fig. 1A). The two layers are separately contacted using a surface-gate depletion scheme (*12*–*14*). The wires, of length L = 17.5 μm and lithographic width 0.17 μm (device A) and 0.18 μm (device B), were squeezed by a negative gate voltage V_{wg}. There is an additional small ungated region p of width 0.9 μm, which provides a current path to the entrances to the 1D wires. The tunneling conductance $G = dI/dV_{dc}$ between the 1D wires and the 2D layer was measured as a function of source-drain bias V_{dc} in an in-plane magnetic field B perpendicular to the wires at lattice temperatures T down to ~40 mK.

First, the effect of the wire-gate voltage V_{wg} was characterized (Fig. 1). Initially, at small V_{wg}, the upper 2DEG screens the lower 2DEG. The first drop in G occurs at −0.40 V when the top well depopulates, leaving narrow 1D wires between the gates. Then, the bottom well is gradually depleted until it pinches off at −0.80 V. B was then swept at each V_{wg} (with V_{dc} = −0.3 mV, to avoid the zero-bias anomaly described later), revealing a series of peaks (Fig. 1B), one pair of peaks at $B_i^{\pm}$ for the ith 1D subband ($i \geq 1$). For this device (A, 0.17 μm wire width), six peaks are observed at V_{wg} = −0.49 V, corresponding to three occupied 1D subbands (*13*). With more negative V_{wg}, the 1D subband spacing increases and the 1D density decreases. Hence, the number of subbands can be reduced to just one. At $V_{wg} \sim -0.65$ V, the wires become insulating. The widths of the wire gates and of the long narrow 2D p region were chosen carefully such that even with just a single 1D subband in the top 2DEG there was minimal modulation of the lower 2DEG and current could still reach the wires. However, the p region inevitably contributes a 2D-2D parasitic tunneling current that appears in the measurements, but this is small and independent of the tunnel current from the wires, even after wire pinch-off, so it can be measured and allowed for.

We now choose V_{wg} = −0.62 V, well into the region where there is just one 1D subband. Figure 2, A and B, shows G as a function of the dc interlayer bias (V_{dc}) and B as color-scale plots, at high (1 K) and low (~40 mK) lattice temperatures, respectively. In the absence of interactions, there should be peaks in G that track the 1D and 2D parabolic dispersion relations; these are indicated with dashed and solid black curves, respectively. The parasitic 2D-2D tunneling in the ungated p region is also shown, as green dash-dotted lines labeled p. The crossing points along $V_{dc} = 0$ occur at $B^- = 1.08$ T and $B^+ = 3.62$ T (Fig. 2B). The 1D Fermi wave vector is $k_{F1D} = ed(B^+ - B^-)/2\hbar$, giving the approximate electron density in the wires $n_{1D} \cong 40\ \mu m^{-1}$ (from $k_{F1D} = \pi n_{1D}/2$). The up-turned (dashed) parabola maps the energy of the 1D wires as a function of wave vector k.

The curves drawn in Fig. 2 are those expected for single-particle tunneling. However, there is an additional region of high conductance to the right of B^+. It drops off along a straight line moving diagonally up and to the left from B^+ (indicated with an arrow). To show this more clearly, the data are differentiated with respect to B and plotted in Fig. 2C. We have taken detailed data in this region, sweeping B, in another device (B) in the same single-subband regime (Fig. 3B). We find a region of large negative dG/dB along a straight line to the right of the high-conductance region; this appears dark blue and is indicated by

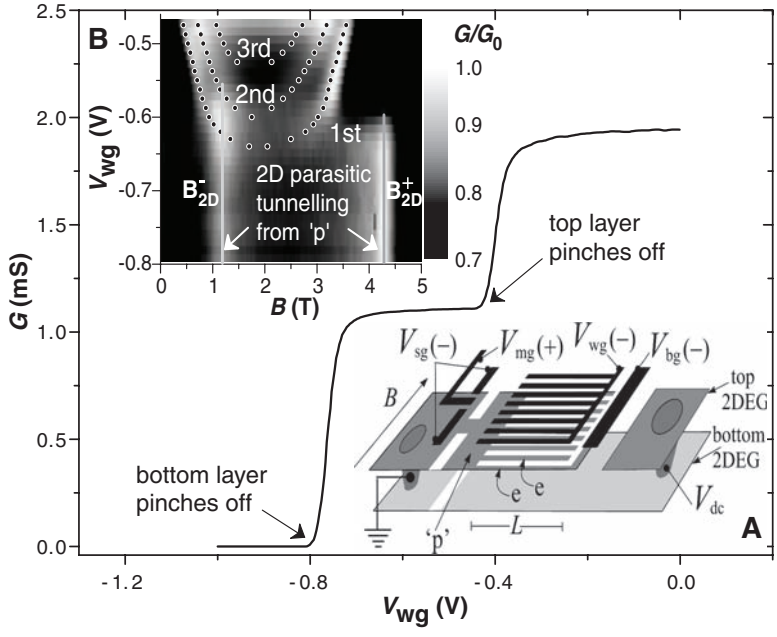

Fig. 1. The conductance, G, as a function of the wire-gate voltage V_{wg} (device A) with no other gates defined. It shows that the strip joining all the wire gates together (see inset A) is depleted at −0.4 V, blocking conduction along the top layer; electrons then have to tunnel to the bottom layer, which is only depleted at −0.8 V. (**Inset A**) Device layout showing gate positions in black; the signs beside the voltage symbols indicate the polarity of the various gate voltages. Current is injected into both layers at the left Ohmic contact, then three gates pinch off the lower layer so that electrons flow into the wires in the upper layer, tunnel to the lower 2DEG and then to the right contact. (**Inset B**) Gray-scale plot of the tunneling conductance showing resonant peaks (bright) as a function of transverse magnetic field measured at a lattice temperature of ~40 mK, with each trace normalized by the maximum height G_0. The dots indicate the features corresponding to the first, second, and third 1D subbands, as labeled, measured from the raw data. The 2D parasitic tunneling from region p does not change with V_{wg}. Its peaks stay at $B^-_{2D} = 1.27$ T and $B^+_{2D} = 4.31$ T, as indicated with vertical solid lines.

the red dashed line. We compare this with the theoretical prediction for noninteracting electrons, shown in Fig. 3A, where a similar dark blue feature also occurs. However, the latter tracks the 1D parabola along its length. In contrast, the feature in Fig. 3B disperses away from the 1D parabola. Because features in the conductance reflect singular features in the spectral function, we can conclude that the 1D parabola and the red dashed line track the dispersion of two independent excitations, which in the TLL framework correspond to the spinon and holon, for spin and charge excitations, respectively.

To confirm this interpretation, we have calculated the tunneling spectra for a TLL coupled to a 2D system of electrons. The framework for these calculations already exists in the literature (*15*, *16*), so we only describe the relevant details here. To compute the tunneling current, we require the spectral function of a TLL, which in general depends on four parameters: the spinon and holon velocities v_σ and v_ρ, respectively, plus two exponents γ_σ and

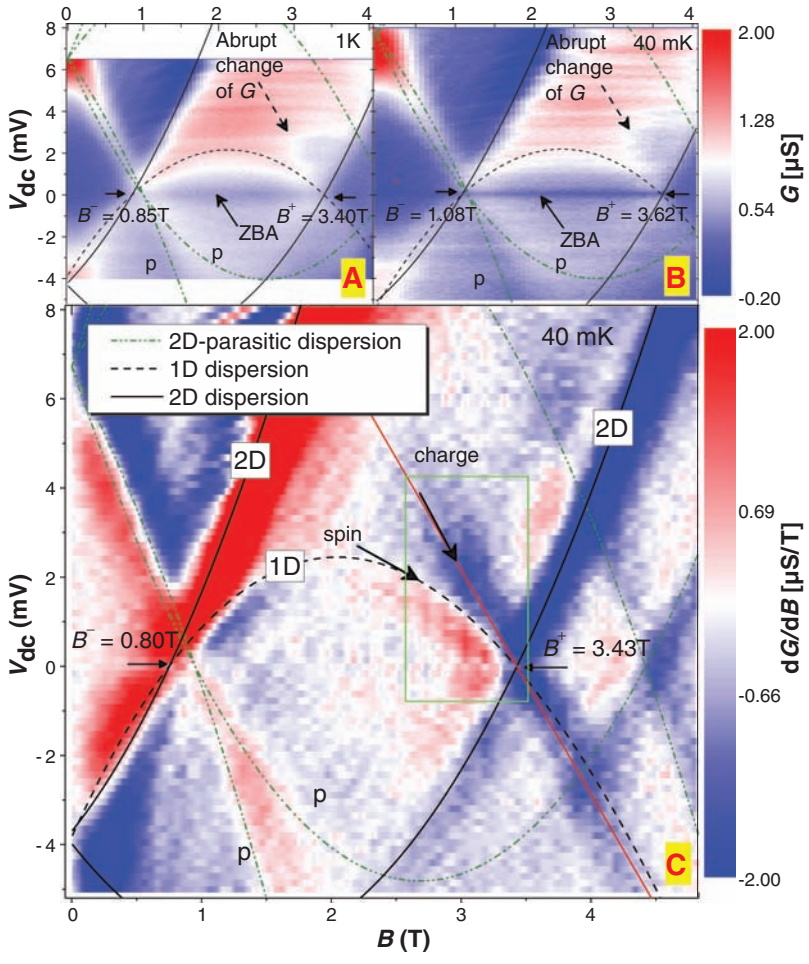

Fig. 2. (**A** and **B**) Color-scale plots of G versus V_{dc} and B at lattice temperatures of 1 K and 40 mK, respectively (device A, for V_{wg} = −0.62 V). Black lines (solid and dashed) indicate the locations of singularities predicted by the noninteracting model for tunneling between the wires and the 2DEG, whereas the green dash-dotted lines indicate the locations of the singularities associated with the parasitic 2D-2D tunneling. There is an additional abrupt decrease in G along the line indicated. In addition, G is suppressed at zero bias, labeled ZBA; this is another sign of interactions. (**C**) dG/dB (device A, for V_{wg} = −0.60 V). The noninteracting parabolae are shown as in (A) and labeled 1D or 2D to indicate which dispersion is being probed. The straight red line indicates the locus of the abrupt change in G indicated in (A) and (B) and is a factor of ~1.4 steeper than the 1D parabola at V_{dc} = 0. This feature clearly moves away from the 1D parabola. We identify it with the TLL charge excitation (holon), whereas the 1D parabola tracks the spin excitation (spinon).

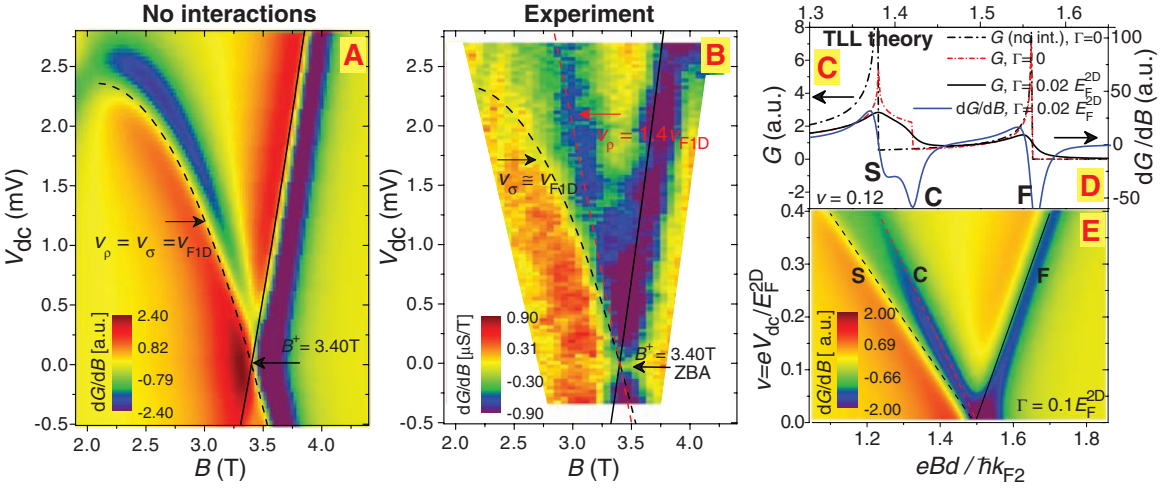

Fig. 3. Comparison of dG/dB for experiment and theory. (**A**) For noninteracting electrons, all features track the noninteracting parabolae (disorder broadening Γ = 0.6 meV). (**B**) dG/dB measured at high resolution while sweeping B, for device B. The red line marks a feature that does not track the noninteracting parabolae and is absent in (A). Calculation of G (**C**) and dG/dB (**D**) for noninteracting electrons and a TLL. The dimensionless bias $v = eV_{dc}/E_F^{2D}$ = 0.12; Γ is indicated for each curve. For the TLL, the spinon velocity $v_\sigma = v_{F1D}$ and the chosen holon velocity $v_\rho = 1.4v_{F1D}$. Spin and charge excitations are labeled S and C, respectively. F labels the noninteracting 2D dispersion curve. (**E**) dG/dB as a function of B and v, showing the same charge feature (C) as in the experiment (B).

γ_ρ. We assume repulsive, spin-rotation-invariant interactions, which implies $\gamma_\sigma = 0$ and $v_\rho > v_\sigma$; in the absence of back-scattering, $v_\sigma \approx v_{F1D}$, the 1D Fermi velocity. For simplicity, we also neglect interbranch scattering processes, which sets $\gamma_\rho = 0$. The spectral function of the 2D system is taken to be a Lorentzian of width Γ, where Γ is the disorder-scattering rate in the 2D system (*17*).

This minimal model is convenient for analytical calculations and is expected to reproduce the main features of the tunneling spectra associated with spin-charge separation. It will not, however, capture the zero-bias anomaly, which is absent for $\gamma_\rho = 0$. Finite γ_ρ is also expected (*16*) to lead to a weakening of the singular features in the spectra, making our calculation the "optimum" case for observing spin-charge separation. Because the TLL model relies on the linearization of the spectrum at low energies, the model's results are only formally applicable in the low-bias part of the spectrum, where this linear approximation holds.

Figure 3C shows the calculated conductance in the vicinity of the B^+ point as a function of scaled magnetic field at fixed voltage for noninteracting electrons, a clean TLL, and a TLL with a little disorder broadening. The singular peak at high magnetic field is independent of the form of the excitations, and hence is common to both systems. The peak at lower magnetic field for the noninteracting system splits, in the TLL case, into a weakened singular peak (which for $v_\sigma = v_{F1D}$ occurs at the same magnetic field as the noninteracting peak), plus a finite discontinuity away from the peak. This sudden drop in the conductance away from the peak is precisely what is observed experimentally in Fig. 2, A and B. Figure 3D shows dG/dB with a little disorder. The spinon is identified as a maximum/minimum pair, which disperse together in the B-V_{dc} plane, as shown in Fig. 3E, for more realistic disorder broadening. The holon is identified as a single minimum, which disperses away from the spinon. We note that an extra feature is also predicted to occur at the B^- point. However, because all three features from this point remain in proximity to each other, it is difficult to resolve them individually.

The experimental results in Fig. 3B are consistent with the predictions in Fig. 3E, at least in the low-bias regime where the linear approximation is reasonable. We have observed this extra feature in the conductance in three devices, at temperatures between ~60 mK and 1.8 K, and on several thermal cycles. We thus conclude that we are observing spin-charge separation, the hallmark of a TLL.

An additional feature that cannot be explained in the noninteracting model is the zero-bias anomaly (ZBA), the strong suppression of conductance along $V_{dc} = 0$, visible as a dark-blue line in Fig. 2, A and B. This is likely to be related to the energy cost for an electron to tunnel into or out of a 1D wire, as it disturbs the line of electrons on either side of it. It has previously been observed in 1D-1D tunneling (*8*), and, for a TLL, G is expected to have identical power-law dependences on V_{dc} and temperature T.

Figure 4A shows the ZBA in the tunneling conductance G as a function of V_{dc} at various T, at a field midway between B^- and B^+. Figure 4, B and C, shows $G(V_{dc} = 0,T)$ and $G(|V_{dc}|, T < 70$ mK), respectively, on log-log plots. Both clearly vary as power laws, as labeled, over considerably more than one order of magnitude. The corresponding power-law exponents $\alpha_T \approx 0.45 \pm 0.04$ and $\alpha_V \approx 0.52 \pm 0.04$ are very similar, as expected. To illustrate that temperature and bias play a similar role in smearing the energy, $G(|V_{dc}|)$ is plotted in Fig. 4D as a function of $V'_{dc} = \sqrt{|V_{dc}|^2 + (3k_BT/e)^2 + V_{ac}^2}$, the simplest way of adding forms of energy smearing together as noise in quadrature. ($3k_BT$ is an estimate of the thermal energy spread, and the factor of 3 is chosen to match the offset between the curves in Fig. 4, B and C.)

The TLL is characterized by the "anomalous" exponent γ_ρ and the spinon and holon velocities. γ_ρ can be expressed in terms of an interaction parameter g [$\gamma_\rho = (g + 1/g - 2)/8$], which indicates the strength of the interactions ($g = 1$ for noninteracting particles). Accurate a priori calculation of g cannot be done in general. However, an estimate based on the 1D densities used suggests $g \sim 0.7$ (supporting online text). We now determine g from the various experimental results.

In TLL theory, the spin velocity v_σ is approximately equal to the Fermi velocity v_{F1D} for weak backscattering ($v_\sigma < v_{F1D}$ for stronger interactions) (*18*, *19*). Thus, the spin mode should follow the low-bias part of the noninteracting 1D parabola (or even lie below it). The charge mode should propagate faster than the spin mode for repulsive interactions. Thus, we label the curve that follows the 1D parabola "spin" and the extra line "charge." For device B, we deduce the velocities close to zero bias to be $v_\sigma \approx v_{F1D} = \hbar k_F/m_{1D} = 1.13 \times 10^5$ ms^{-1} and $v_\rho \approx 1.4\ v_{F1D}$, respectively. In a Galilean invariant system, $g = v_{F1D}/v_\rho$ (*19*), so this gives $g \approx 0.7$, which is consistent with the estimate given above. For device A, g is very similar to that of device B, as is the 1D electron density. Another device, with a thinner (7 nm) barrier, yields $g \approx 0.65$.

Within TLL theory, the power-law exponents extracted from the ZBA can also be directly related to g. The form of the exponent depends on whether the excitations are affected by the ends of the wire. This is determined by comparing the energy of the tunneling electron to $\Delta E = 2\hbar v_{F1D}/gL$, which is related to the inverse time scale for the holon to travel to the end of a

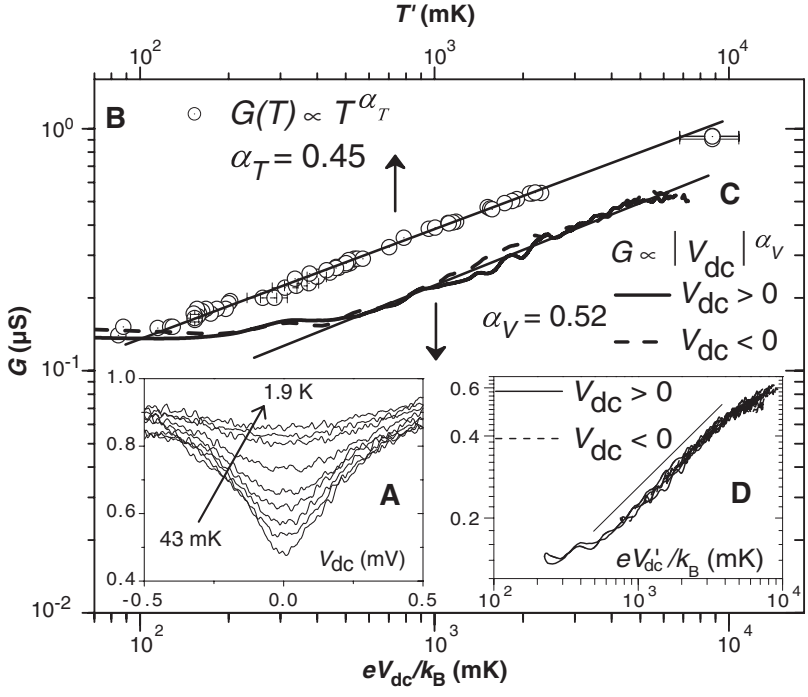

Fig. 4. The dependence of the conductance G on bias V_{dc} and temperature T (device B). (**A**) The ZBA at various T up to 1.9 K at $B = 2.33$ T. (**B**) Minima of the ZBA [$G(V_{dc} = 0)$] versus T. G varies as T^{α_T}, where $\alpha_T \approx 0.45$ over nearly two orders of magnitude. (**C**) $G(|V_{dc}|)$ on a log-log plot (with V_{dc} scaled to temperature using $eV_{dc} = k_BT$), on scales matching those in (B) for T, showing that it varies as $V_{dc}^{\alpha_V}$, where $\alpha_V \approx 0.52$ over more than one order of magnitude. (**D**) $G(|V_{dc}|)$ versus $V'_{dc} = \sqrt{|V_{dc}|^2 + (3k_BT/e)^2 + V_{ac}^2}$, the simplest way of adding the forms of energy smearing together as noise in quadrature. The value $3k_BT$ is chosen to superpose the lines in (B) and (C) and also all the curves in (D), where the lowest temperature has been adjusted from 43 mK to 70 mK to avoid saturation. Using the more complex scaling relation of equation 5 of (*3*) also gives a universal curve if $\alpha \approx 0.51$.

wire of length L (*8*, *20*). For $k_BT, eV_{dc} >> \Delta E$, the ends are unimportant and the process is called "bulk" tunneling, with an exponent $\alpha_{bulk} = (g + 1/g - 2)/4$. Taking $L = 17\mu m$ and $g = 0.7$ gives $\Delta E \approx 150$ mK for our device, and therefore almost all of our ZBA data shown in Fig. 4 are expected to be in the bulk-tunneling regime. The measured values of $\alpha_T = 0.45$ and $\alpha_V = 0.52$ (device B) give $g \approx 0.28$ and 0.26, respectively.

The values of g found from the ZBA exponents are much smaller than that extracted from the holon branch in Fig. 3. We briefly offer possible explanations for this [with more detail in (*14*)]. One possibility is that impurities and imperfections may make the effective length of each wire shorter than the lithographic length. It is well known that an impurity in a TLL will effectively cut it into two at low energies. Although at finite energies, electrons are able to tunnel through such constrictions, one might expect that the constrictions will modify the form of the ZBA exponent in a similar way to "ends." If we use the formula for ZBA exponent in the end-tunneling regime (*14*), the extracted values of g (0.53 from α_T and 0.49 from α_V) are more comparable to that extracted from the holon branch.

Alternatively, it may not be valid to extrapolate the higher-energy properties of the branches to low energies where the ZBA is measured. The interactions between the wires and/or between the wires and the 2DEG may become important, and may alter the form of the ZBA exponent (*21*). The effective dielectric constant of the material may also be energy dependent, changing the strength of the interactions at low energies.

TLL theory is based on the assumption of a linear dispersion relation about the Fermi energy. We go beyond that regime at high dc bias. There is very little work on interactions in 1D wires at high energy where the TLL approximation breaks down. Haldane (*1*) argued that all 1D metals are adiabatically continuous with the TLL, that is, perturbations such as the band curvature are only expected to lead to a renormalization of the TLL parameters, so spin-charge separation should persist; this is backed up by recent renormalization-group calculations (*22*). Recent theoretical work on spinless fermions for a curved band has shown an intriguing interplay of Fermi-liquid and TLL behavior (*2*, *23*). Numerical calculations have been performed in this regime (*24*) using quantum Monte Carlo methods, with results that resemble our experimental results—a parabolic spin branch and a fairly straight charge branch.

References and Notes

1. F. D. M. Haldane, *J. Phys. C Solid State Phys.* **14**, 2585 (1981).
2. A. Imambekov, L. I. Glazman, *Science* **323**, 228 (2009).
3. M. Bockrath *et al.*, *Nature* **397**, 598 (1999).
4. A. M. Chang, M. K. Wu, C. C. Chi, L. N. Pfeiffer, K. W. West, *Phys. Rev. Lett.* **86**, 143 (2001).
5. C. Kim *et al.*, *Phys. Rev. Lett.* **77**, 4054 (1996).
6. B. J. Kim *et al.*, *Nat. Phys.* **2**, 397 (2006).
7. P. Segovia, D. Purdie, M. Hengsberger, Y. Baer, *Nature* **402**, 504 (1999).
8. Y. Tserkovnyak, B. I. Halperin, O. M. Auslaender, A. Yacoby, *Phys. Rev. B* **68**, 125312 (2003).
9. O. M. Auslaender *et al.*, *Science* **295**, 825 (2002).
10. O. M. Auslaender *et al.*, *Science* **308**, 88 (2005).
11. B. Kardynal *et al.*, *Phys. Rev. Lett.* **76**, 3802 (1996).
12. S. A. Nield, J. T. Nicholls, W. R. Tribe, M. Y. Simmons, D. A. Ritchie, *J. Appl. Phys.* **87**, 4036 (2000).
13. Y. Jompol *et al.*, *Physica E* **40**, 1220 (2008).
14. Materials and methods are available as supporting material on *Science* Online.
15. A. Altland, C. H. W. Barnes, F. W. J. Hekking, A. J. Schofield, *Phys. Rev. Lett.* **83**, 1203 (1999).
16. S. A. Grigera, A. J. Schofield, S. Rabello, Q. Si, *Phys. Rev. B* **69**, 245109 (2004).
17. N. Turner *et al.*, *Phys. Rev. B* **54**, 10614 (1996).
18. J. Voit, *Phys. Rev. B* **47**, 6740 (1993).
19. C. E. Creffield, W. Häusler, A. H. MacDonald, *Europhys. Lett.* **53**, 221 (2001).
20. C. L. Kane, M. P. A. Fisher, *Phys. Rev. B* **46**, 15233 (1992).
21. D. Carpentier, C. Peça, L. Balents, *Phys. Rev. B* **66**, 153304 (2002).
22. H. Benthien, F. Gebhard, E. Jeckelmann, *Phys. Rev. Lett.* **92**, 256401 (2004).
23. M. Khodas, M. Pustilnik, A. Kamenev, L. I. Glazman, *Phys. Rev. B* **76**, 155402 (2007).
24. M. G. Zacher, E. Arrigoni, W. Hanke, J. R. Schrieffer, *Phys. Rev. B* **57**, 6370 (1998).

25. We acknowledge the UK Engineering and Physical Sciences Research Council for funding. Y.J. was supported by a scholarship from the Thai Ministry of Science. We thank F. Sfigakis for experimental assistance and B. E. Kardynal and C. H. W. Barnes for useful discussions.

Supporting Online Material

www.sciencemag.org/cgi/content/full/325/5940/597/DC1
Materials and Methods
SOM Text
References

3 February 2009; accepted 6 May 2009
10.1126/science.1171769

The Formation of Population III Binaries from Cosmological Initial Conditions

Matthew J. Turk,[1]* Tom Abel,[1] Brian O'Shea[2]

Previous high-resolution cosmological simulations predicted that the first stars to appear in the early universe were very massive and formed in isolation. Here, we discuss a cosmological simulation in which the central 50 $M_\odot$ (where $M_\odot$ is the mass of the Sun) clump breaks up into two cores having a mass ratio of two to one, with one fragment collapsing to densities of 10^{-8} grams per cubic centimeter. The second fragment, at a distance of ~800 astronomical units, is also optically thick to its own cooling radiation from molecular hydrogen lines but is still able to cool via collision-induced emission. The two dense peaks will continue to accrete from the surrounding cold gas reservoir over a period of ~10^5 years and will likely form a binary star system.

Hydrodynamical simulations that start from cosmological initial conditions have predicted that the first luminous objects in the universe were isolated stars with masses in the range of 30 to 300 $M_\odot$ (where $M_\odot$ is the mass of the Sun) on the basis of accretion rates calculated in the absence of accretion-inhibiting factors (*1*–*3*). Idealized protostellar evolution simulations suggest that accretion should end when the star reaches ~100 $M_\odot$ (*4*), but although most relevant feedback mechanisms of the protostars on their accretion flow are known (*5*), no fully self-consistent radiation hydrodynamical simulations reaching the main sequence have yet been possible, even in one dimension. The early stages of protostellar evolution, however, are understood in some detail from spherically symmetric calculations (*6*, *7*) as well as semi-analytic models (*8*).

The environment in which the first stars form is calculated by following early-universe evolution of the primordial gas and dark matter; by this means, the first stars are found to form in halos with a total mass of ~10^6 $M_\odot$, with collapse driven first by cooling via molecular hydrogen rovibrational lines and later by collision-induced emission (*6*, *9*, *10*). Although several tens of calculations (*1*, *11*, *12*) have followed the collapse of a primordial protostellar halo to relatively low densities (~10^{-12} g cm^{-3}), only two previous calculations have followed the collapse from cosmological initial conditions to protostellar densities (*2*, *13*). Both of these calculations used a chemical model that included the relevant medium- and high-density physics, such as heating from the formation of molecular hydrogen, collisionally induced emission, three-body molecular hydrogen formation, and gas opacity at high densities. Several simulations have followed the collapse of a single metal-free cloud starting from idealized initial conditions (*3*, *14*, *15*). Parameter studies of rotating cylinders have shown that metal-free gas can fragment (*16*) and have found fragmentation of spherical distributions of extremely low- and zero-metallicity gas (*17*), including in three-dimensional nested grid parameter studies (*18*). Additionally, studies of zero-metallicity gas collapsing in isolation have found fragmentation at low densities (~10^{-16} g cm^{-3}) (*19*). However, no previous simulation starting from cosmological

[1]Kavli Institute for Particle Astrophysics and Cosmology, Stanford University, 2575 Sand Hill Road, Menlo Park, CA 94025, USA. [2]Department of Physics and Astronomy, Michigan State University, East Lansing, MI 48824–2320, USA.

*To whom correspondence should be addressed. E-mail: mturk@slac.stanford.edu